Materials Science & Engineering A 841 (2022) 142989

Contents lists available at ScienceDirect

Materials Science & Engineering A

journal homepage: www.elsevier.com/locate/msea

Correlation between tensile properties, microstructure, and processing routes of an Al–Cu–Mg–Ag–TiB_2 (A205) alloy: Additive manufacturing and casting

M. Avateffazeli [a], P.E. Carrion [b,c], B. Shachi-Amirkhiz [d,e], H. Pirgazi [f], M. Mohammadi [e], N. Shamsaei [b,c], M. Haghshenas [a,*]

[a] Failure, Fracture and Fatigue Laboratory (F3L), Department of Mechanical, Industrial, and Manufacturing Engineering, University of Toledo, OH, USA
[b] Department of Mechanical Engineering, Auburn University, Auburn, AL, 36849, USA
[c] National Center for Additive Manufacturing Excellence (NCAME), Auburn University, Auburn, AL, 36849, USA
[d] CanmetMATERIALS, Natural Resources Canada, 183 Longwood Road South, Hamilton, ON, L8P 0A5, Canada
[e] Marine Additive Manufacturing Centre of Excellence (MAMCE), University of New Brunswick, Fredericton, NB, Canada
[f] Department of Electromechanical, Systems and Metal Engineering, Ghent University, B9052, Ghent, Belgium

ARTICLE INFO

Keywords:
Additive manufacturing
Laser powder bed fusion
Al–Cu–Mg–Ag–TiB_2
A205
Yield point phenomenon
PLC effect
Discontinuous yielding

ABSTRACT

This paper aims at assessing microstructure/processing route/mechanical property correlation of a high-strength TiB_2/Al–Cu–Mg–Ag aluminum alloy, namely A205 alloy, additively manufactured via laser powder bed fusion (LPBF) versus the cast counter material. To this end, high magnification advanced microstructural characterization in connection with the tensile flow and strain hardening (i.e., work hardening) behavior of the materials were studied. Ambient temperature uniaxial tensile tests, based on ASTM E8/E8M, were conducted on the LPBF and cast as well as post-heat treated (T7: overaged and stabilized) materials were performed systematically. Results show a pronounced discontinuous yielding for the LPBF material along with extended ductility. The tensile curve of the LPBF T7 heat-treated material showed some plastic instabilities (Portevin–Le Chatelier effect) in the inelastic region. However, none of these phenomena were observed in the cast material, while ductility is limited. These responses were attributed to the very high cooling/solidification rates experienced by the LPBF materials, which result in a very fine equiaxed and supersaturated aluminum grain structure as compared with the coarse-grained structure of the cast counter material.

1. Introduction

Precipitation-hardened aluminum alloys, with a great strength-to-weight ratio, can be considered good candidates for various high-demand and lightweight engineering applications [1]. Among various precipitation-hardened aluminum casting alloys, the TiB2/Al–Cu–Mg–Ag, known as A205 alloy, is a recently developed commercial alloy with enhanced castability (e.g., reduced level of casting shrinkage) and strength properties [2,3]. This alloy possesses one of the highest ultimate tensile strength values of aluminum cast alloys along with excellent high-temperature creep properties owing to the existence of thermally stable TiB2 particles within its microstructure [4].

In the cast state, the optimum strength of the A205 alloy can be reached through T7 heat treatment (T7 HT), which is a precipitation hardening heat treatment (HT) in Al–Cu casting alloys. As a result of the T7 HT, the alloy can reach an overaged (or past peak strength) condition without considerable cold working (also sometimes referred to as stabilized). The significant enhancement in the strength of the A205 casting material is achieved through the formation of some plate-like finely dispersed Al_2Cu precipitates [5], with similar chemical composition but different habit planes that can effectively hinder dislocation motion. The T7 cycle is rather complex as it includes a six-step solution heat treatment followed by a four-step artificial aging process [6].

The A205 alloy has been recently commercially offered for the laser powder bed fusion (LPBF) process producing an ultrafine-grained structure with enhanced mechanical properties relative to the cast counter material [7,8]. A state-of-the-art approach in the LPBF of

* Corresponding author.
E-mail address: meysam.haghshenas@utoledo.edu (M. Haghshenas).

https://doi.org/10.1016/j.msea.2022.142989
Received 5 January 2022; Received in revised form 8 March 2022; Accepted 12 March 2022
Available online 25 March 2022

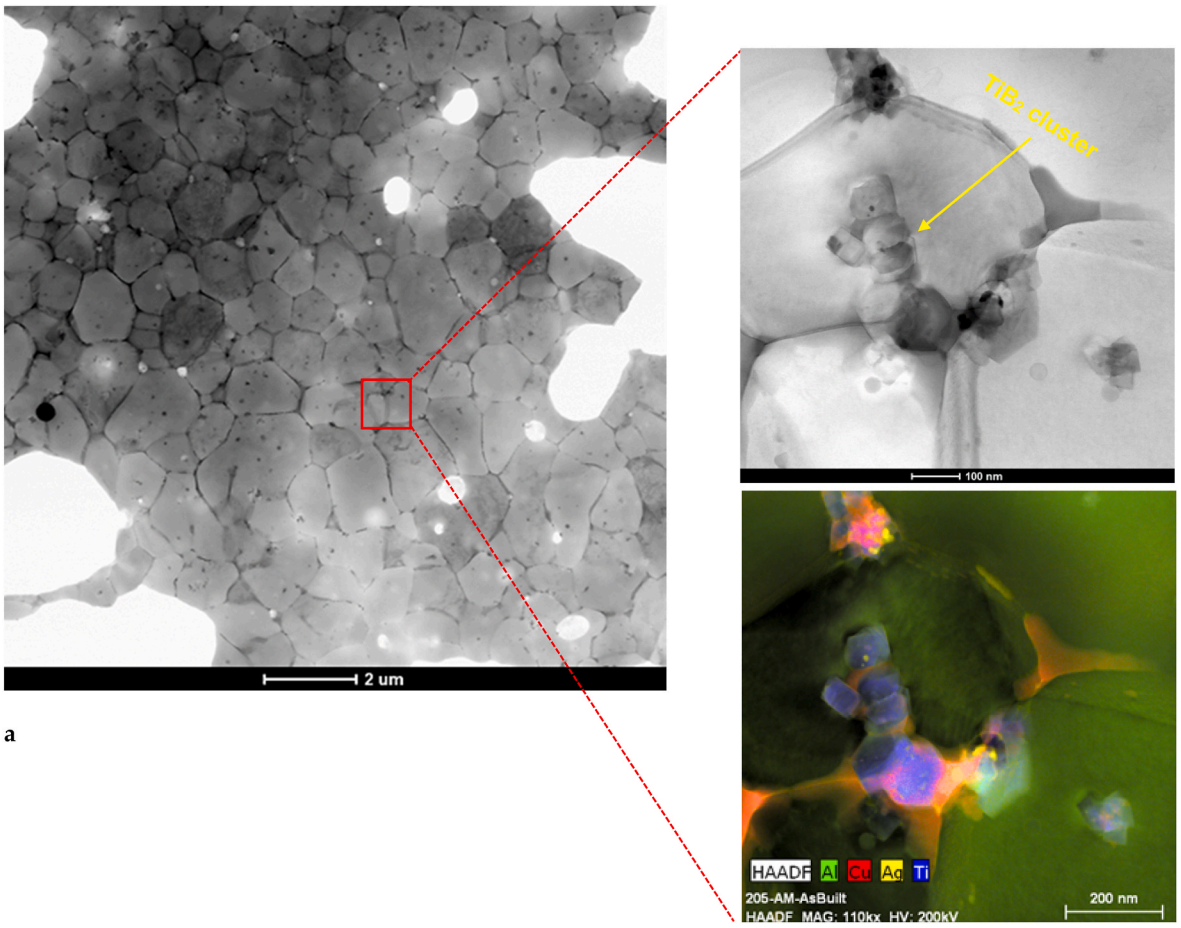

Fig. 1. STEM-BF images and STEM-EDX mapping of the starting microstructures of the LPBF materials; a) LPBF A205 (as-built), b) LPBF A205 (T7 HT). Clusters of TiB_2 nanoparticles and different Al_2Cu precipitates are visible in the as-built and T7 HT materials, respectively.

high-strength aluminum alloys (like Al–Cu alloys) is to "modify" the microstructure of the material by adding thermally stable ceramic-based nanoparticles. To this end, A205 alloy can be considered an aluminum matrix composite reinforced with thermally stable (melting temperature ~3230 °C) TiB2 nanoparticles (as the most-used grain refiner in aluminum alloys) [9]. The TiB2 nanoparticles not only control the grain size and morphology (i.e., ultrafine/equiaxed) but also can enhance the toughness (strength and ductility) of the material. Other elements such as Ag can develop the high-temperature capability of A205 alloy, while Cu and Mg expedite the precipitation hardening of the alloy [8,10]. The enhanced ductility that results from grain refinement is strongly reliant on the distribution of nanoparticles and the volume fraction of reinforcements in the material. The well-dispersed TiB2 nanoparticles would most likely pin the grain boundary structure. Pinned grain boundaries can act as effective barriers against small crack growth due to the crystallographic misorientations around them. Therefore, fracture development during plastic deformation is postponed and is prevented from spreading. Due to the presence of TiB2 nanoparticles and TiB2 clusters inside the matrix, TiB_2 particle-rich zones can also deviate the growing cracks and therefore contribute to the ductility of the structure [9,11].

Recently, Ghoncheh et al. [12] reported the tensile flow behavior of the LPBF A205 alloy and observed a serrated flow (shortly after yielding) and yield point phenomenon in the material; however, Ghoncheh et al. [12] did not conduct a comprehensive review on the tensile flow behavior of the alloy. The serrated flow behavior was also reported by Mair et al. [13,14] in the LPBF nano-CaB_6 reinforced 2024 aluminum and TiB_2 modified Al–Cu alloys. Biffi et al. [8] investigated the microstructure, processability, and mechanical properties of LPBF TiB_2/Al–Cu and reported plastic instability and jerky flow behavior of the alloy as well with no in detail discussion. Nie et al. [15] observed Portevin-Le Chatelier (PLC) effect in the LPBF Zr-modified Al–Cu–Mg–Mn alloy. They attributed the PLC effect to the grain refinement induced by the Zr and precipitation of Al3Zr. The enhanced tensile strength and the yield point phenomenon were observed by Zhang et al. [16] on Zr-modified Al–Cu–Mg alloy as well. Recently Hu et al. [17] conducted a comprehensive study on the aging response of LPBF Al–Cu alloys and compared the microstructure/texture, and tensile response of as-built as well as various aged A205 materials. The aging cycle employed by Hu et al. [17] included solution treatment + natural aging and solution treatment + artificial aging (at different times and temperatures). Hu et al. [17] reported the PLC effect only in the as-built A205 material. Upon the

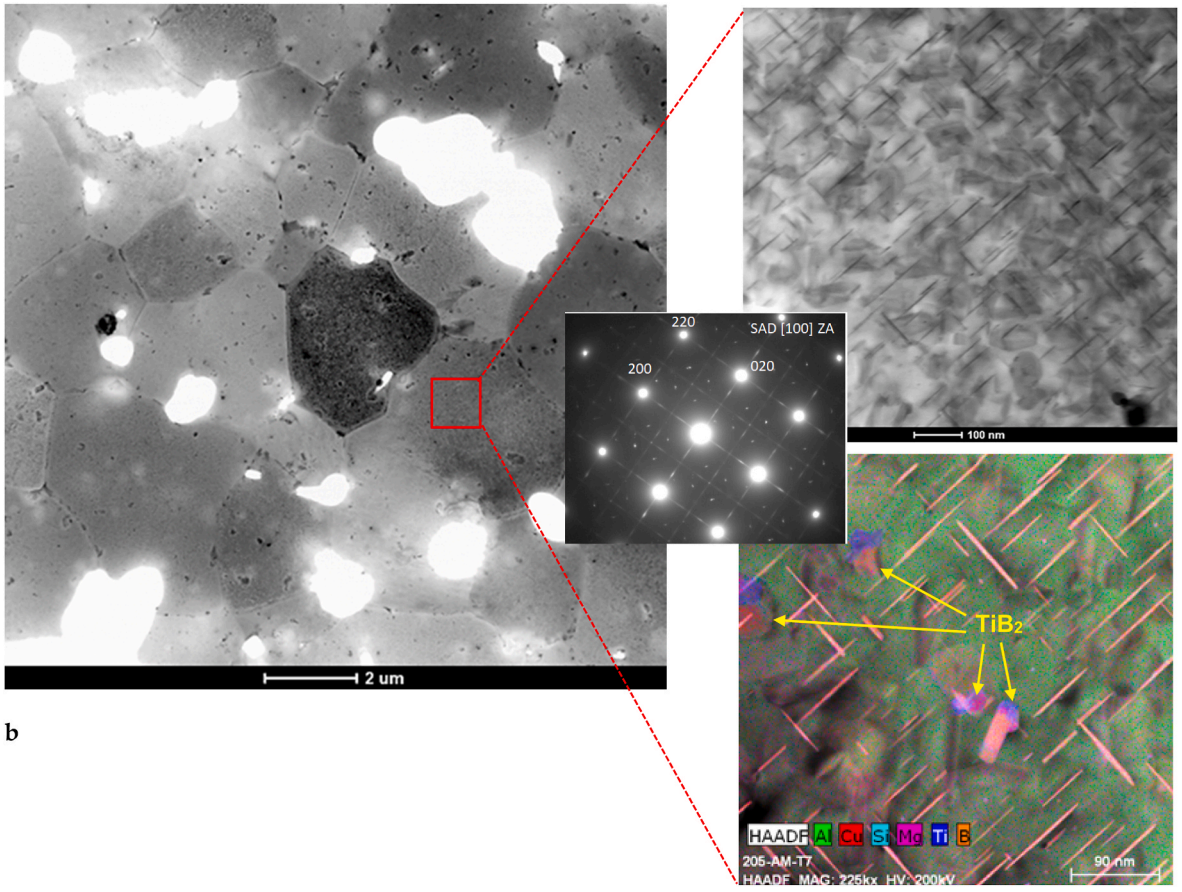

Fig. 1. (*continued*).

mentioned post-heat treatments, they described a simultaneous increase in both strength and ductility with no PLC phenomenon confirming the importance of post-fabrication heat treatment of the additive manufactured Al–Cu alloys.

Through the correlations between microstructure and mechanical properties of LPBF A205 alloy have been established recently, there is a tangible lack of knowledge on detailed characterization of tensile properties in the as-built and T7 HT condition of this alloy as compared with the cast counter materials (as cast and post-T7 HT). Therefore, this study tends to correlate the tensile properties, including work hardening and fracture behavior of LPBF and cast A205 materials (i.e., as cast, as-built, and T7 HT) with advanced microstructural measures including transmission electron microscopy and scanning electron microscopy-based fractography. We would like to know how tensile properties would vary with the processing routes of casting versus LPBF (e.g., solidification rate) and heat treatment. This then would lead us to understand the potential governing mechanisms of plastic deformation as well as the type of fracture behavior (ductile and/or brittle) of the materials.

2. Experimental procedure

The casting A205 aluminum was produced by mixing preheated potassium fluorotitinate (K_2TiF_6) and potassium fluoroborate (KBF_4) inorganic salts into melted Al–Cu–Mg–Ag alloy in an atomic ratio corresponding to the Ti/B and the desired TiB_2 content of the alloy. Ti and B atoms released from the salt exothermic reaction forms TiB_2 according to $K_2TiF_6 + 2KBF_4 \rightarrow TiB_2 + 4\,KF + 5F_2$. To get the as-cast ingot, the slag needs to be brushed from the top of the melt as thoroughly as possible.

The A205 powder is produced by atomizing the Al–Cu–Mg–Ag–TiB_2 molten material. To this end, Materials Solution Ltd (UK) employed A205 powder with particle sizes ranging from 20 to 63 μm (D10 = 21.78 μm, D50 = 39.16 μm, and D90 = 55.44 μm to manufacture the samples. The particle size distribution has been precisely designed to meet the needs of all powder bed fusion machines. The A205 samples were laser powder bed fused using an EOS M290 machine with 350 W power, 80 μm laser spot size, 50 μm layer thickness, 1000–2000 mm/s scan speed, and 0.05–0.10 mm hatch distance.

4.65Cu-3.41Ti-1.45B-0.60Ag-0.20Mg-0.08Si-0.06Fe (all numbers are weight percentage) is the nominal chemical composition of an LPBF A205 sample analyzed by inductively coupled plasma optical emission spectroscopy (ICP-OES).

Cast A205 samples were fabricated by the investment casting method, in which the alloy was induction melted and poured at 800 °C via Sedex 30 ppi filters into investment casting ceramic molds at 200 °C. One separate group of the LPBF and cast samples was T7 heat treated (solutionizing and stabilizing/over-aging).

Tensile tests were performed using an MTS Landmark equipped with a 100 kN load cell in strain-controlled mode up to 5% strain amplitude

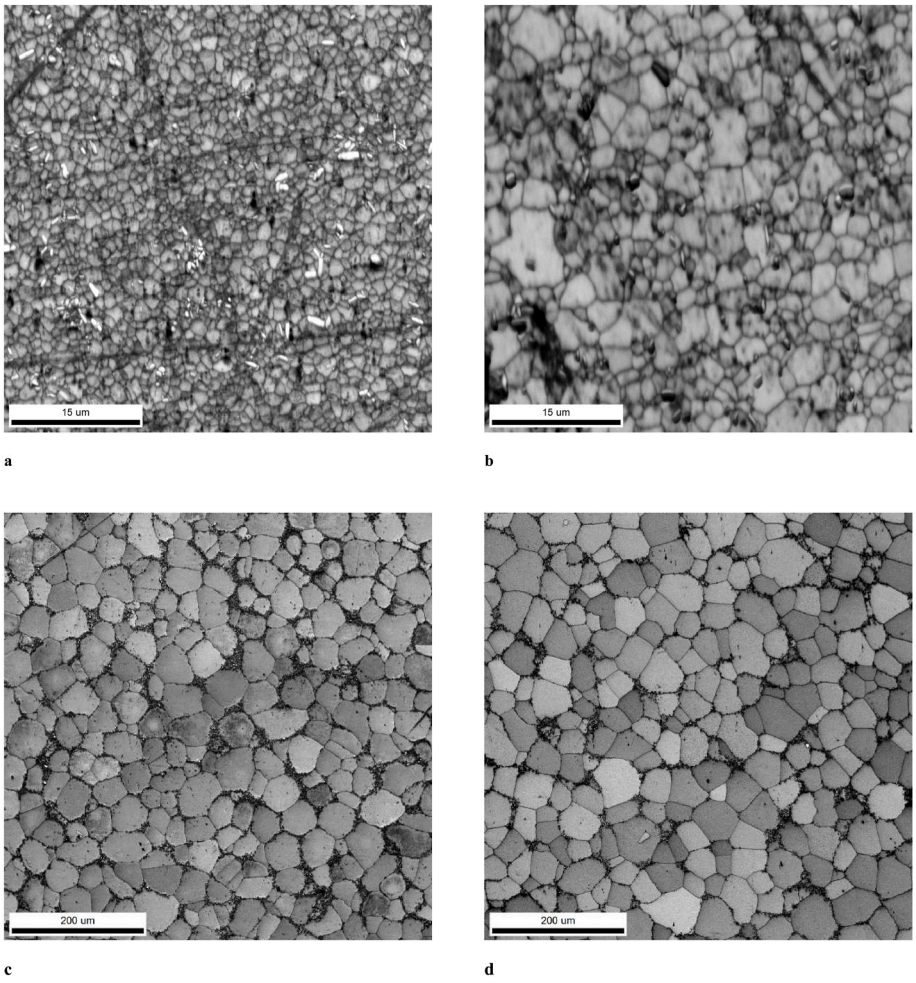

Fig. 2. SEM micrographs of the starting microstructures of the LPBF and cast materials; a) LPBF A205 (as-built), b) LPBF A205 (T7 HT), c) cast A205 (as-cast), d) cast A205 (T7 HT).

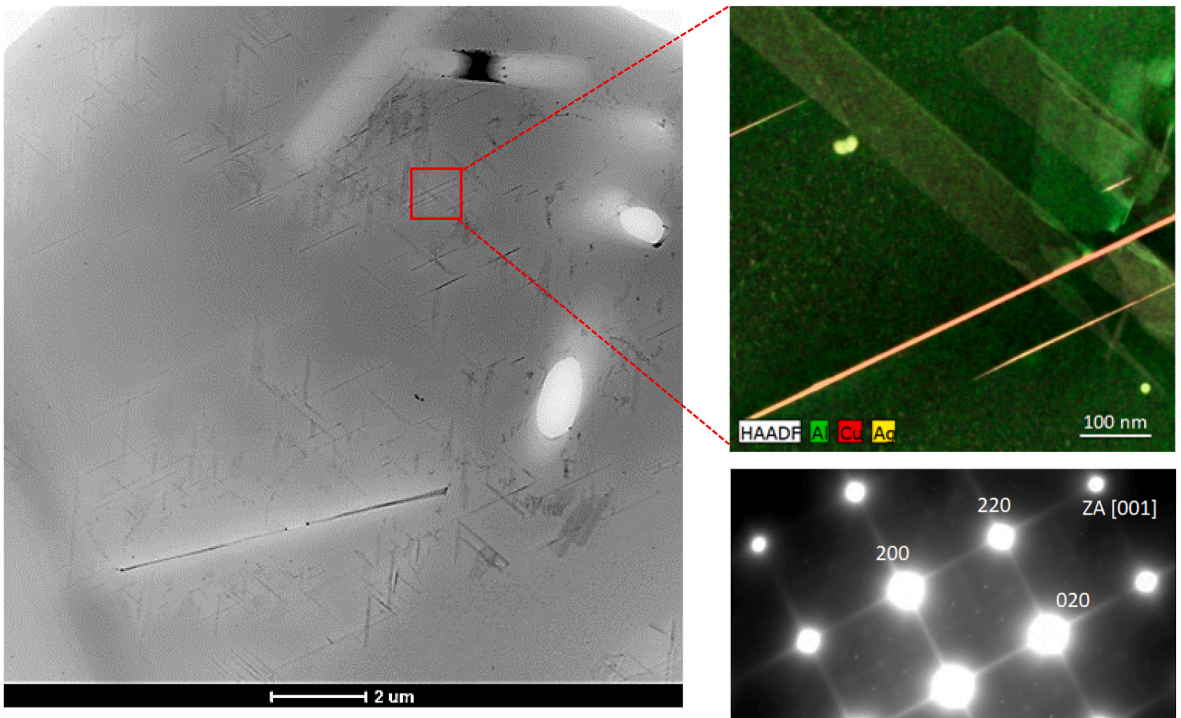

a

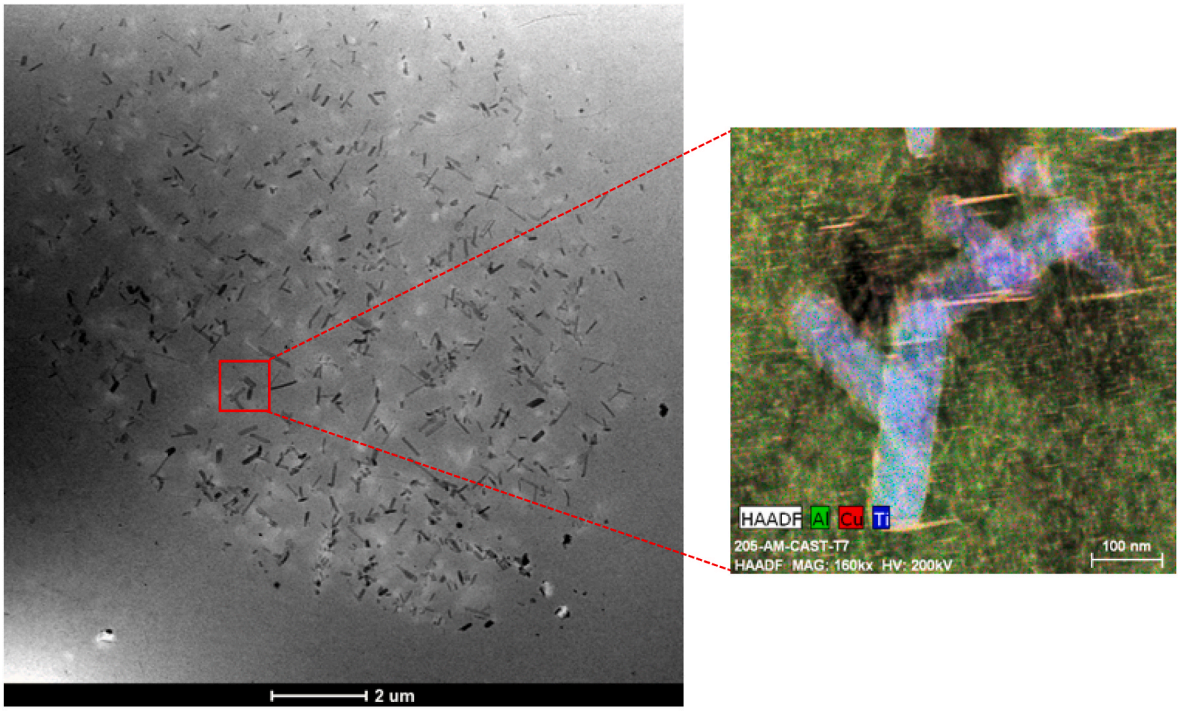

b

Fig. 3. STEM-BF and STEM-EDX mappings of the cast materials; a) cast A205 (as-cast), b) cast A205 (T7 HT). The diffraction pattern of the as-cast samples are included in Fig. 3a. The dispersoid shown in Fig. 3b is Ti–Si rich.

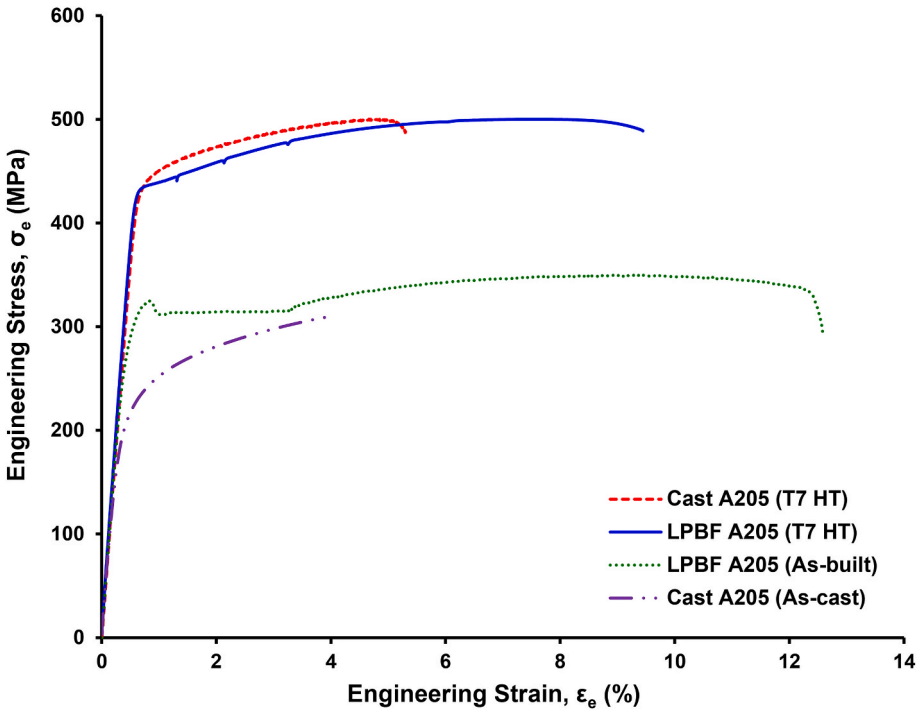

Fig. 4. Engineering tensile flow curves of the studied cast and LPBF A205 materials.

Table 1
Measured grain size, yield stress (YS), ultimate tensile strength (UTS), and percentage of elongation (El%) of the studied materials.

Materials	Grain size (μm)	YS (MPa)	UTS (MPa)	El%
Cast A205 (as-cast)	46.4 ± 13.5	215 ± 1.6	295 ± 5.5	4.1% ± 1.5
Cast A205 (T7 HT)	48.5 ± 10.7	441 ± 1.4	501 ± 6.7	5.3% ± 1.6
LPBF A205 (as-built)	1.1 ± 0.4	309 ± 1.5	350 ± 1.7	12.5% ± 1.1
LPBF A205 (T7 HT)	3.5 ± 1.6	440 ± 1.7	483 ± 2.4	9.5% ± 1.3

and continued in displacement-controlled mode up to fracture (strain rate was 0.001 mm/mm/s) according to ASTM E8. The strain was measured with a 10 mm gauge length extensometer. Tensile tests were performed three times in each condition to ensure the repeatability of the tensile data.

A Hitachi S-4800 UHR scanning electron microscope (SEM) was employed to conduct fractography assessments of the tensile test fractured samples. Using a TenuPol twin-jet electro-polisher, electron-transparent samples were prepared for TEM investigations by electro-polishing 3-mm disks punched from thinned foils. TEM observations were performed using an FEI Tecnai Osiris operating at 200 kV, equipped with a SuperEDS X-ray detection system used for chemical analysis.

3. Results and discussion

3.1. Starting microstructures

In this section, we broadly assess the high magnification microstructure and microstructural features of the studied LPBF and cast materials. Fig. 1 shows scanning transmission electron microscopy bright-field (STEM-BF) images of the LPBF materials, i.e., Fig. 1a: LPBF A205 (as-built) and Fig. 1b: LPBF A205 (T7 HT). As seen, the α-aluminum grains show no preferential orientation (they are equiaxed) with the average sizes of 1.1 ± 0.4 μm and 3.5 ± 1.6 μm for the LPBF A205 (as-built) and LPBF A205 (T7 HT), respectively. The zoomed-in image in Fig. 1a shows the clusters/agglomerates of TiB_2 nanoparticles on grain boundaries. These nanoparticles contribute greatly to the formation of refined grains in the microstructure of LPBF A205 (as built) through pinning the grain boundaries and acting as nucleation sites for the new grains [12,18]. The zoomed-in image in Fig. 1b shows a higher magnification STEM-BF image within an α-aluminum grain of the LPBF A205 (T7 HT) material. Some thin plate-like Al_2Cu precipitates, at different orientations, are seen within the grains. These precipitates do not exist in the as-built material confirming their presence due to the T7 heat treatment. We assess these precipitates extensively throughout this paper.

Upon preliminary assessment of the microstructure of the cast materials, we figured out that grains are significantly coarser than the ones in the LPBF A205 (as-built and T7 HT) materials. To this end, the STEM-BF images, exclusively, may not necessarily provide comprehensive images of the cast microstructure (including grains and grain boundaries). Therefore, for the assessment of the grain structures in the cast material, first, the SEM was employed to see the overall distribution and morphology of grains, see Fig. 2 (Fig. 2a: cast A205 (as cast) and Fig. 2b: cast A205 (T7 HT)). The α-aluminum grains are equiaxed and some distribution of the TiB_2 and Al_2Cu particles/crystals formed and segregated at the grain boundaries is evident. Upon scanning the microstructures several times, to make sure the collected measures are representative of the whole microstructure, the average grain size of cast A205 (as cast) and cast A205 (T7 HT) were measured as 46.4 ± 13.5 μm and 48.5 ± 10.7 μm, respectively. It is seen the T7 heat treatment changes neither the grain size nor the morphology of the grains in cast materials widely. The pointedly coarser grain size of the cast materials

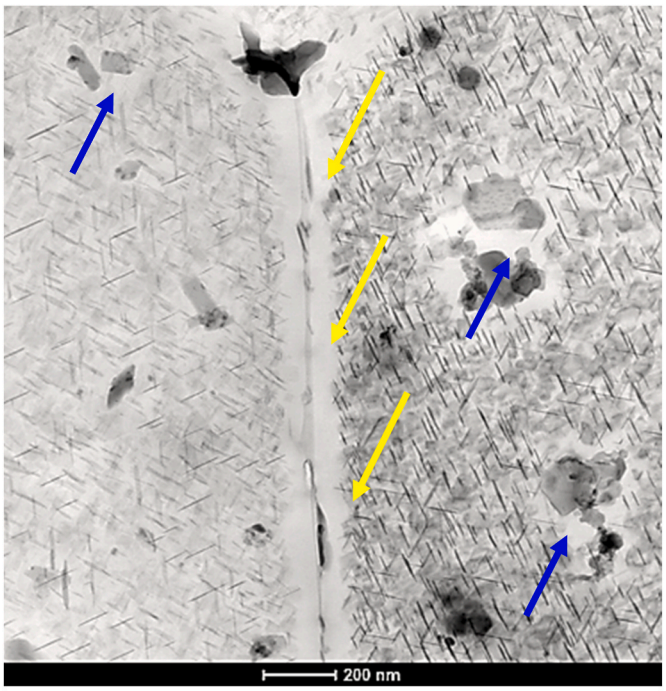

A

b

Fig. 5. STEM-HAADF image showing: a) the presence of PFZs on grain boundaries (yellow arrows) and around the TiB_2/Al_2Cu particles (blue arrows) in the microstructure of the LPBF A205 (T7 HT), and b) the absence of the PFZs the microstructure of the cast A205 (T7 HT). **(For interpretation of the references to colour in this figure legend, the reader is referred to the Web version of this article.)**

relative to the LPBF materials is mainly due to dissimilar cooling/solidification rates in the processes (i.e., very high cooling rate in the LPBF process relative to the relatively low cooling rate of the casting processes). Upon completion of the SEM studies of the cast microstructures, the STEM-BF images were recorded with a small region within the individual (coarse) grains. Fig. 3 shows the STEM-BF of the α-aluminum grains (inside the grain) in cast A205 (as cast), Fig. 3a, and cast A205 (T7 HT), Fig. 3b. Some coarse Cu-rich precipitates containing Ti can be observed in the α-aluminum grains of the cast A205 (as-cast) microstructure.

3.2. Stress-strain flow behavior

Fig. 4 demonstrates the engineering stress-strain curves of all studied materials and conditions. For the sake of comparison, Table 1 summarizes the 0.2% offset stress, the UTS, the elongation, and the grain size numbers of the materials.

Considering the flow curves of the cast A205 (as-cast) and LPBF A205 (as-built) samples, the absence of typical strength-ductility compromise is clear in the as-built material; i.e., the LPBF A205 (as-built) shows higher strength and ductility relative to the cast A205 (as-cast) material. This is an indication that the randomly oriented equiaxed fine grain structure of the LPBF A205 (as-built) is promising to enhance ductility and strength simultaneously. Since the diffusion distance between TiB_2/Al_2Cu particles/precipitates that segregate mainly on grain boundaries is shorter when grains are finer, homogenization of the microstructure in the LPBF A205 (as-built) material takes less time. Due to the homogenous distribution of equiaxed grains, e.g., absence of coarse grains grown epitaxially, when a tensile load is applied, the grains experience a more uniformly distributed deformation with no (or less) strain localization, unlike what is seen in structures with columnar grains like LPBF AlSi10Mg alloys [19,20]. As a result, there is a higher degree of deformation coordination compatibility, which reduces the risk of early crack nucleation during tensile deformation [21].

The LPBF A205 (as built) material shows a *yield point phenomenon* (upper yield point followed by an extended plateau of yielding up to about 3% strain) with a low work hardening rate. Unlike the casting process with a cooling rate of 1–100 °C/s, the LPBF induced very high solidification/cooling rates (10^3–10^6 °C/s) allow for a substantially larger extension of Ti and Cu supersaturating into the Al matrix. At room temperature, the equilibrium value of soluble Ti in α-aluminum is near zero. However, under the very high cooling rate of the LPBF process (non-equilibrium condition), Ti remains in supersaturated aluminum in the range of 0.48–0.53 wt% [12,14]. This results in enhanced pinning of dislocations due to elastic field interaction between the solute atoms (solute trapping) in the supersaturated α-aluminum and the moving dislocations. Indeed, differences in the shear modulus and atomic size of Cu and Ti solute atoms with the aluminum matrix (shear moduli of Ti, Al, and Cu are 43 GPa, 25 GPa, and 46 GPa, respectively) may create local strain fields that interact with moving dislocations and limit their free motions along slip planes [11]. With the continuation of the straining (or increasing the applied tensile stress), dislocations would be released, and the stress level suddenly drops until dislocations are stuck again by the solute atoms [14,15]. This mechanism directly contributes to the observed yield point phenomenon in the LPBF A205 (as-built) material.

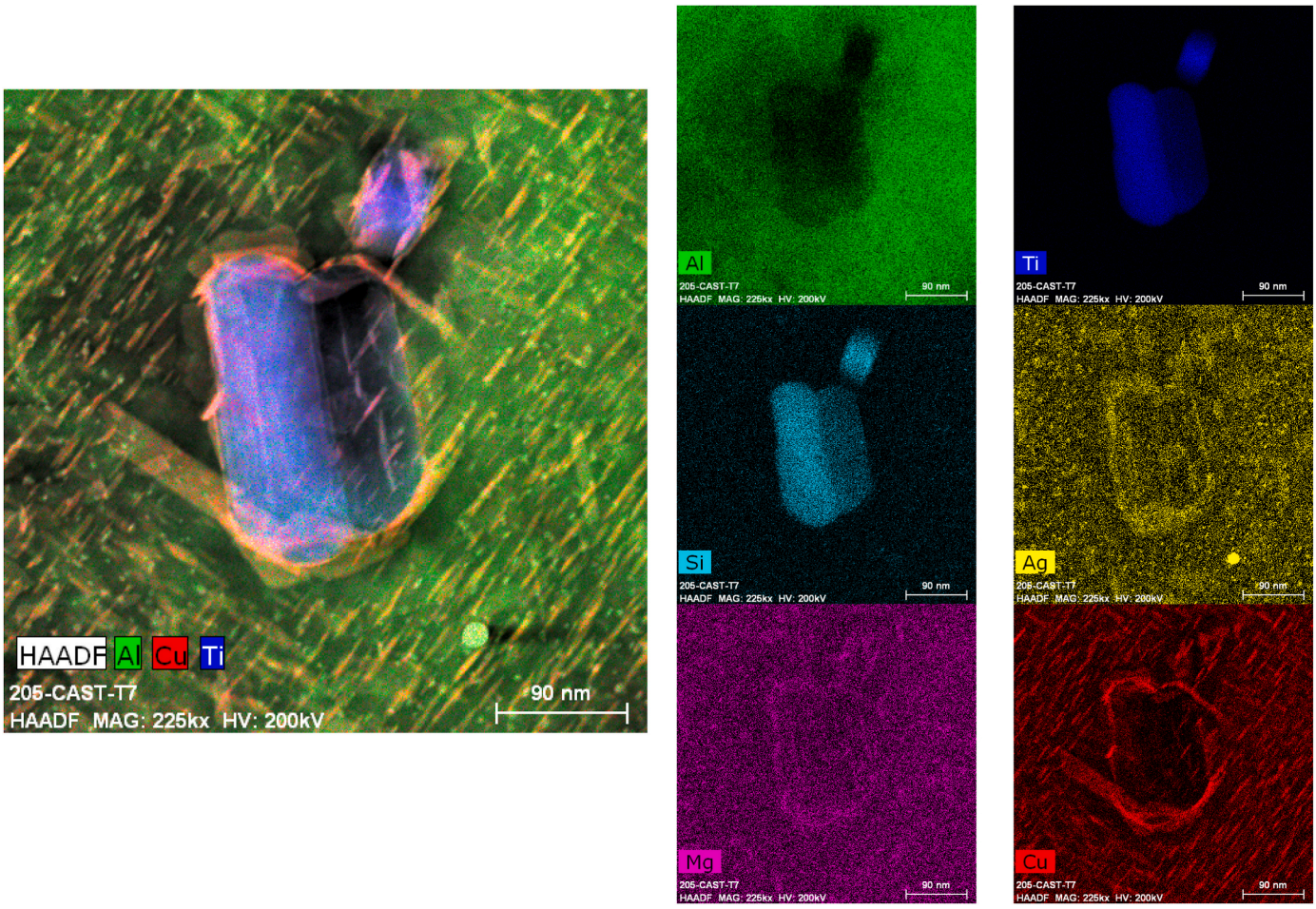

Fig. 6. HAADF image and elemental mapping of the observed Ti–Si rich dispersoids/intermetallic in the cast A205 (T7 HT) sample.

3.3. Correlation between the flow properties and the microstructure evolution

The contribution of TiB_2 nanoparticles on the strengthening of the as-built material can be summarized as Orowan strengthening via distributed nano-TiB_2 particles, grain boundary pinning (fine grains), and load-bearing reinforcement due to interfacial bonding between nano-TiB_2 particles and the aluminum matrix [8,14,22]. The nanosize-TiB_2 particles can also act as heterogeneous inoculants for new dislocations and new grains. This is mainly due to stiffness and thermal coefficient mismatch between the TiB_2 particles and the aluminum matrix.

Upon subjecting LPBF A205 to T7 HT, the overall strength improves compared with the as-built condition. Though the average grain size in the LPBF A205 (HT T7) condition, 3.5 ± 1.6 μm, is about four times larger than the LPBF A205 (as-built) material, 1.1 ± 0.4, the enhanced strength of the LPBF A205 (HT T7) material is attributed to the strengthening precipitates including plate-like Ω precipitates on the {111} matrix planes. These precipitates were identified considering the habit planes and the lattice parameters reported in our previous works [12,18]. Upon T7 heat treatment, the sequence of precipitation in the Al–Cu–Mg–Ag alloy system is SSSS[1]→GP zone→θ''→θ'→θ (Al_2Cu), and SSSS→ Mg–Ag co-cluster → Ω (Al_2Cu) [23]. That is, two phases of plate-like Ω (on the {111} Al habit planes), and θ'/θ'' (on the {001} Al habit planes) precipitate in the microstructure [24,25]. It is reported that both Ω and θ' precipitates are formed simultaneously with similar chemical compositions though their habit planes are different. The {111} plane, being the principal glide plane in the face-centered cubic aluminum matrix, the hexagonal-shaped plate-like Ω (Al_2Cu) precipitates effectively impede the dislocation glide and therefore largely contribute to the strengthening of the LPBF A205 (HT T7) alloy. The presence of silver (Ag) in the A205 alloy would greatly contribute to the formation of the Ω precipitates [14,26]. Indeed, Ag acts as an efficient trap for Mg atoms to form Mg–Ag co-clusters. The formation of Mg–Ag co-clusters, during the early stages of the T7 aging, acts as heterogeneous nucleation sites for Ω precipitates. It has been reported that the addition of Ag in Al–Cu–Mg alloys suppresses the precipitation of the θ′ phase while encouraging the dense precipitation of the Ω phase, resulting in a significant improvement in the age-hardening level [27]. A unique feature of the Ω precipitate is its resistance against coarsening (i.e., being thermally stable) contributing efficiently to the strengthening of the material. That is, to complete the relocation of the thickening ledges, the high aspect ratio of the Ω-phase plates necessitates extra time for the rearrangement of Ag and Mg atoms along the flat surfaces of this phase [28,29]. Considering the LPBF A205 (T7 HT) material, limited plastic instabilities (drop in the continuous smooth plastic flow) are observed, which are due to the impact of the moving dislocations and

[1] SSSS: supersaturated solid solution.

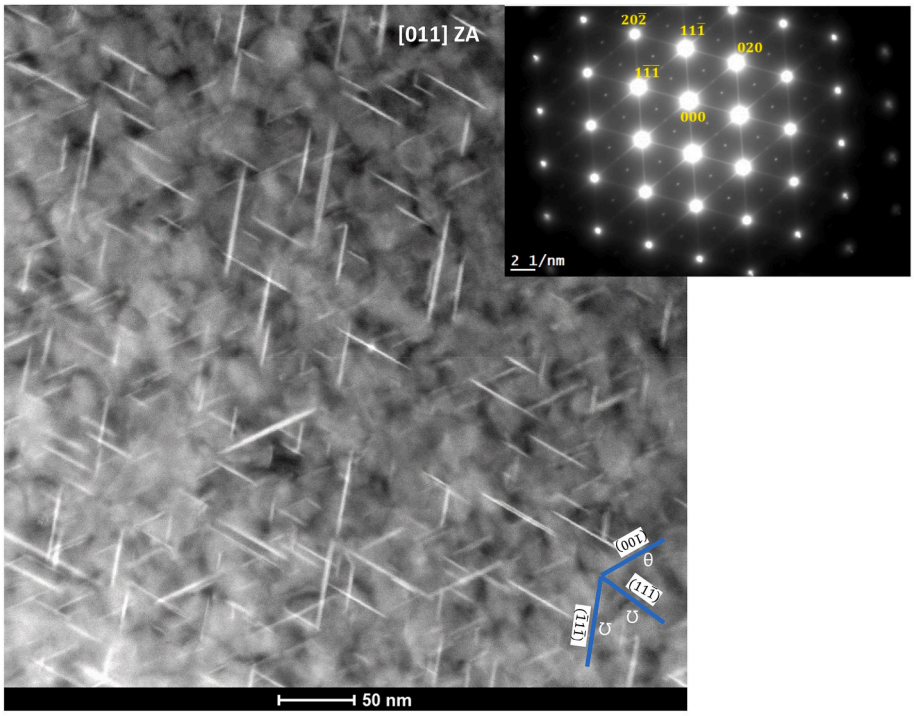

a

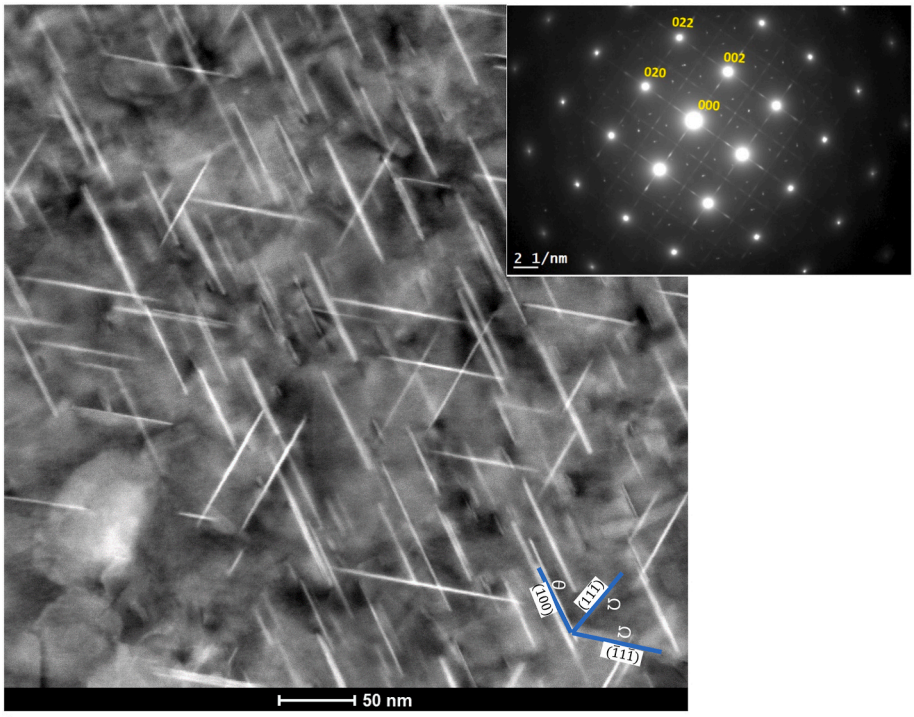

b

Fig. 7. STEM-HAADF images of finely dispersed thin plates of θ′ and Ω in; a) cast A205 (T7 HT), b) LPBF A205 (T7 HT). Included in this figure are diffraction spots. In Fig. 7b, Ω phase diffraction spots at (1/3){022} and (2/3){022} are observed.

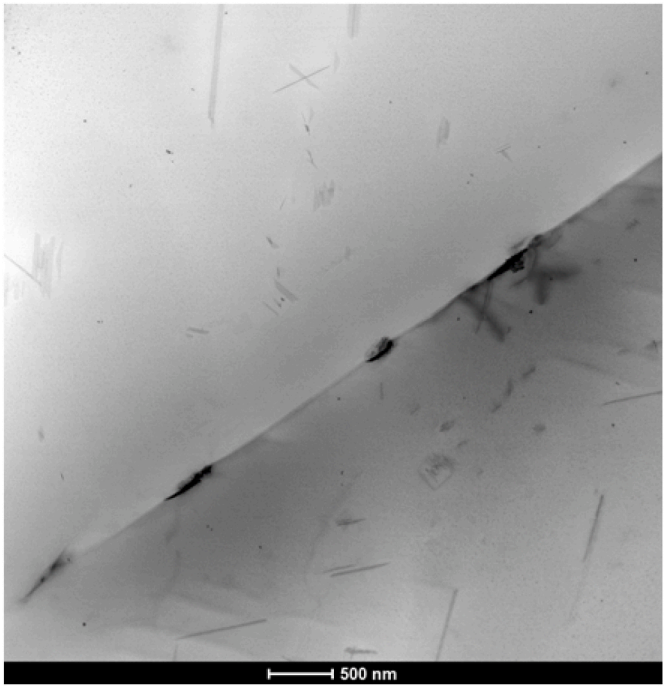

Fig. 8. STEM-BF images of the cast A205 (as-cast) showing two grains (partially) and coarse/discrete precipitates on the grain boundaries.

diffusing solute atoms on each other. That is, the instability of the dislocations can result in the instability of the strain flow which exhibits itself as serrations in the stress-strain curves. The decrease in dislocation density, due to dynamic recovery, in the LPBF A205 (T7 HT) material results in the mentioned limited instabilities in the flow curve. However, it is observed that the LPBF A205 (T7 HT) material is still more energy absorbent per se (can accommodate more plastic deformation than the cast materials) even after the ductility reduction when compared to the as-built one. In other words, the enhanced ductility of the as-built material can be credited to the finer grain size of the material in which (*i*) stress concentration can be effectively reduced and (*ii*) the large density of grain boundaries allows the material to accommodate more plastic deformation before final fracture. These give rise to the extended ductility of the fine-grained LPBF A205 materials [30,31] as compared with the cast counter materials.

The reasons for the absence of the yield point phenomenon can be attributed to (*i*) a reduction in the solute concentration in the aluminum matrix; in other words, the α-aluminum matrix is to a lesser extent supersaturated and therefore no (or less) dynamic interaction occurs between moving dislocations and Cu/Ti solute atoms, (*ii*) an overall reduction in the density of dislocations due to the annihilation of dislocations (dynamic recovery) induced by the T7 heat treatment, and (iii) consumption of Cu during the precipitation of the Ω-phase, resulting in a progressive depletion of Cu from the supersaturated solid solution [32].

Comparing the mechanical properties of LPBF A205 (as-built) and cast A205 (as-cast), enhanced strength and ductility are observed for the LPBF material with the LPBF A205 (as built) being the most ductile and cast A205 (as cast) being the least ductile (most brittle) ones. The enhanced mechanical properties of the LPBF A205 (as-built) relative to the cast A205 (as cast) material can be attributed to the ultrafine grain size of the as-built material relative to the coarse grain microstructure of the as-cast material. The refined grain size of the LPBF A205 (as-built) material, 40 times smaller, and the solid solution strengthening in the LPBF material relative to the cast counter material contribute effectively to the higher strength and ductility of as-built material relative to the as-cast counter material. However, as seen in Table 1, the UTS of the cast A205 (T7 HT) material is slightly higher than the LPBF A205 (T7 HT) while its elongation is 44% lower. This is interesting because the grain size of the cast A205 (T7 HT) material (48.5 ± 10.7 μm) is significantly larger than the LPBF A205 (T7 HT) counter material (3.5 ± 1.6 μm), while the difference in strength is not that significant. Therefore, the slightly higher strength of the cast A205 (T7 HT) material, as compared with the LPBF A205 (T7 HT) counter material is not because of the Hall-Petch effect. This can be justified through the fact that the density of grain boundaries in the LPBF A205 (T7 HT) is largely more than the cast A205 (T7 HT) material; on the other side, grain boundaries act as sinking regions for vacancies upon which strengthening precipitates would nucleate heterogeneously. That is, precipitates cannot form in the vicinity of the grain boundaries (due to a lack of vacancies as nucleation sites), even if the matrix may be supersaturated with the solute atoms. Therefore, it is expected (and well documented) to realize precipitate free zones (PFZs) on (or in the vicinity) of grain boundaries and/or around TiB_2/Al_2Cu crystals [33,34]. The finer grain size of the LPBF A205 (T7 HT) material is equivalent to a higher fraction of grain boundaries (as compared with coarse-grained cast A205 (T7 HT) counter material) which means a higher fraction/density of PFZs within the microstructure. The PFZs are generally detrimental to the mechanical properties as they are soft areas free of solute atoms and/or strengthening precipitates [35,36]. As a result, the creation of PFZs along grain boundaries (and around TiB_2/Al_2Cu particles) would partially counteract (compromise) the strengthening caused by grain refinement in the LPBF A205 (T7 HT) material. Therefore, the mechanical strength of the cast A205 (T7 HT) material is slightly higher than the LPBF A205 (T7 HT) counter material and this can be attributed to a lesser volume of precipitate free zones (PFZs), due to the lower density of grain boundaries in the coarse-grained cast A205 (T7 HT) material. Fig. 5a shows the presence of the PFZs around the grain boundaries (yellow arrows) and the TiB_2 crystals (blow arrow) in the microstructure of the LPBF A205 (T7 HT). However, the similar-magnification STEM-BF image, Fig. 5b, of the counter microstructure of the cast A205 (T7 HT) microstructure does not reveal any PFZs. Some fiber-like features in Fig. 5b are indeed Ti–Si rich dispersoids with Cu, Ag, Mg in minor amounts segregated on the interface (boundary) of the dispersoids, see Fig. 6. It is worth noting that, the observed high content of silicon (Si) is because this element is included in the investment casting process of the Al–Cu–Mg–Ag–Ti–B alloy to enhance the melt fluidity and to refine the grain size.

As briefly mentioned before, the higher strength of the cast A205 (T7 HT) relative to LPBF A205 (T7 HT) material can also be attributed to a larger number density of finer Ω precipitates of the cast material relative to the LPBF counter material, see Fig. 7a and b. These STEM-BF images, taken at the same magnification, show that the Ω precipitates are coarser in the LPBF A205 (T7 HT) material compared with the cast A205 (T7 HT). Also, the number density of Ω phase in the cast A205 (T7 HT) material is higher than the LPBF A205 (T7 HT) counter material, 136/201601 nm^2 as opposed to 41/201601 nm^2.

Cast A205 (as-cast) material shows the least ductility and strength among the studied materials. Considering the STEM-BF images of the

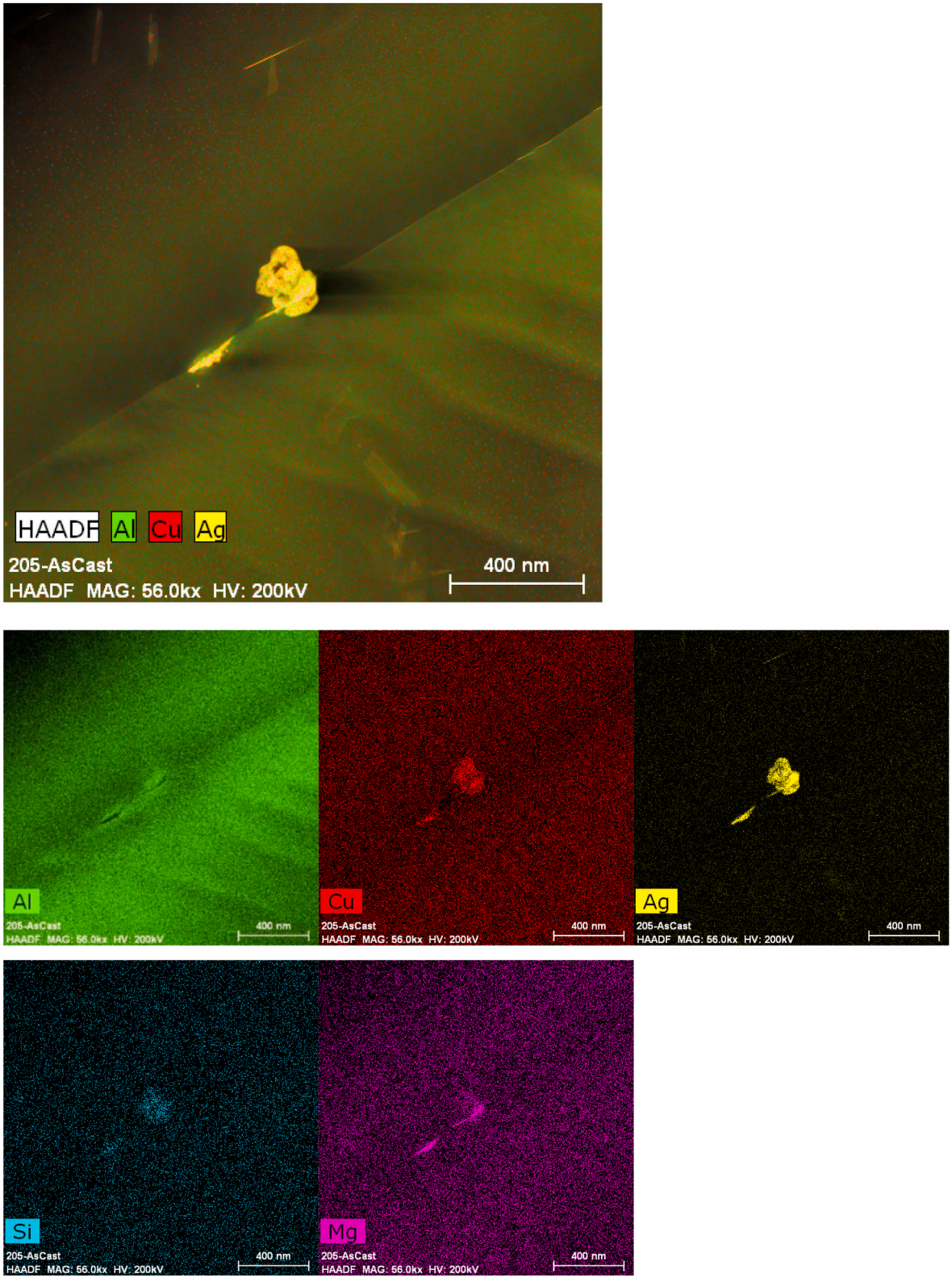

Fig. 9. Elemental mapping of the discrete precipitates on the grain boundaries of the cast A205 (as-cast) material.

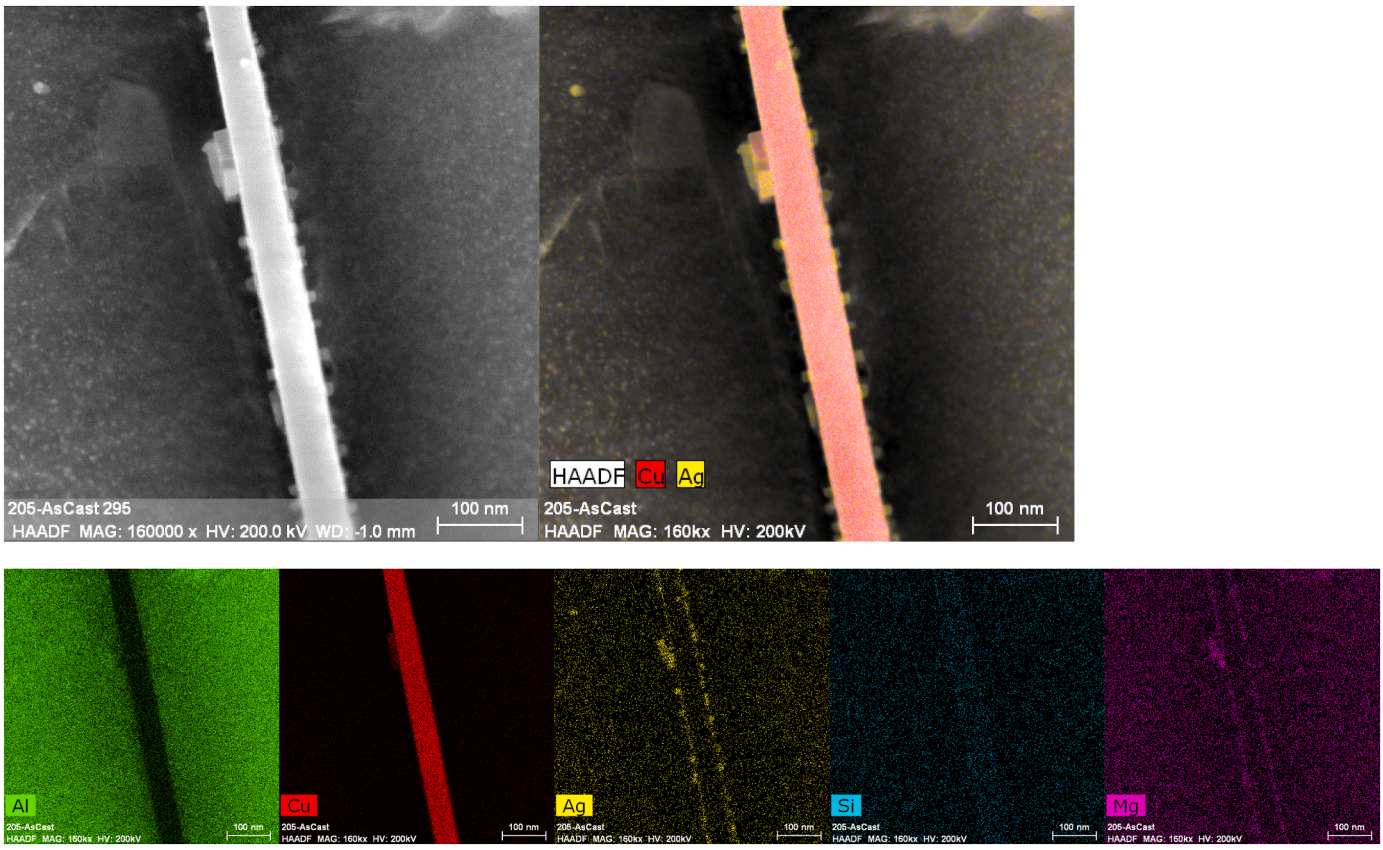

Fig. 10. Coarse (rod-like) Cu-rich precipitates with segregation of the trace elements (Ag and Mg) in the cast A205 (as-cast) material.

cast A205 (as cast), see Fig. 8, some coarse and discrete precipitates were observed on the grain boundaries. Corresponding EDS maps show, see Fig. 9, that these are Cu-rich precipitates comprising Ag and Mg. Due to the presence of these disconnected precipitates at the GBs, stress-tolerance limits of the GBs would be abridged, and this would lower the toughness (strength and ductility) of the cast A205 (As-cast) material. Further on the cast A205 (as-cast) material and indexed along the [001] zone axis (ZA), Fig. 10, we observed coarse (rod-like) Cu-rich precipitates on which silver elements segregate at the interface. It is worth noting that upon post T7 heat treatment, these Ag elements that co-exist with Mg promote the nucleation of the finely dispersed Ω-phases.

3.4. Work hardening rate

To obtain a better perception of the mechanical behavior of the studied LPBF and cast materials, the work hardening rate parameter, ratio of true stress (σ_T), to true strain (ε_T) written as $\frac{\partial\sigma}{\partial\varepsilon}$, versus true strain, ε_T (mm/mm) plots were developed. Fig. 11a shows the true flow curves σ_T-ε_T of the tested materials and Fig. 11b contain the corresponding $\frac{\partial\sigma}{\partial\varepsilon}$- ε_T plots.

The work hardening rate plots show a typical first reduction (elastic/plastic shift [8,37]). In the LPBF A205 (as-built) material, the very low values of the work hardening rate up to about 3% correspond with the initial yield stress plateau. Thereafter, the strain hardening increases over 2000 MPa and then falls until Considère's criterion is fulfilled, suggesting uniform elongation and necking are achieved before the final failure. The work hardening plot of the LPBF A205 (T7 HT) material shows a similar initial drop followed by a continuous decrease along with some sudden jump and drop corresponding with limited instabilities in the uniform plastic domain. Also, there are some serrations visible in the plot of the LPBF A205 (as-built) material, while more intense serrations can be seen for the LPBF A205 (T7 HT) material.

The limited work hardening rate of the LPBF materials can be attributed to notably refined equiaxed grains which lead to higher interaction between dislocations and large density of grain boundaries, as well as a large density of PFZs [11,37]. Due to the presence of a large number of grain boundaries, the generated dislocations, caused by the tensile straining, could not effectively accumulate/store within the grains (i.e., dislocation forest) to enhance the work hardening, i.e., being annihilated by other dislocations and/or swallowed into grain boundaries. In other words, for the LPBF A205 (as-built) material, at the end of the yield plateau (about 3% strain), the generated and accumulated dislocations would effectively be annihilated with a large density of grain boundaries [38,39].

The rate of work hardening, at the early stages of the plastic flow, of the cast materials (as cast and cast-T7) is higher than the LPBF materials. The origin of the work hardening behavior in the A205 cast materials could be linked to stiffness incompatibilities between the matrix (α-aluminum) and the TiB_2 particles (on the α-aluminum grain boundaries) during plastic deformation resulting in some back stress in the matrix [40]. Because the direction of this resistance is opposite of that of the applied stress, it inhibits plastic deformation (e.g., dislocation slide)

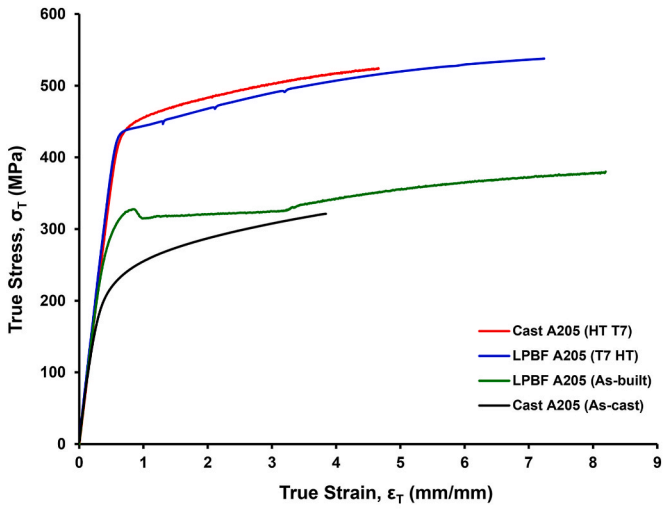

a

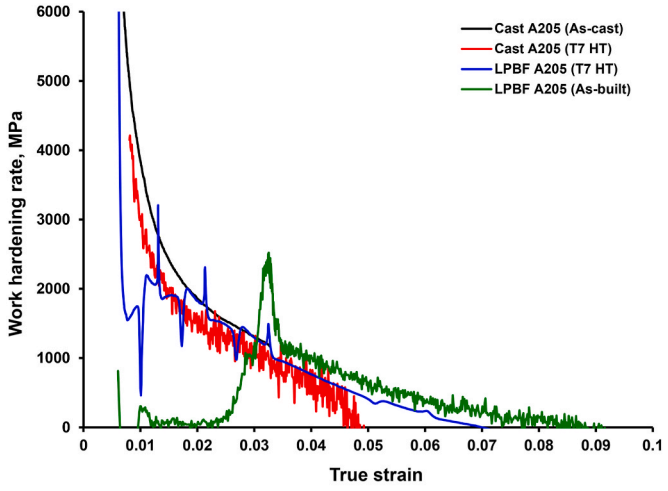

b

Fig. 11. a) True stress-strain curves, b) work hardening rate versus true strain for the studied materials.

and thus contributes to work hardening. Furthermore, the interface between the TiB_2 particles and the α-aluminum matrix, due to their significantly different stiffness and coefficient of thermal expansion, would act as a perfect site for dislocations generation and emission which results in a large local dislocation density and dislocation accumulation. This would eventually obstruct dislocation movement and contribute to hardening through the dislocation forest mechanism. Added to these would be less density of grain boundaries in the coarse-grained cast materials resulting in less probability for dislocations being sunk in (swallowed by) the grain boundaries. Also, the lower density of grain boundaries in the cast material is equal to the lower possibility of PFZs' occurrence.

3.5. *Fractography assessments*

To better assess the nature of the tensile fracture and the features of the fracture surface, extensive SEM fractography studies were performed on the LPBF and cast materials. Fig. 12 shows the SEM images of the tensile fracture surfaces of the LPBF A205 materials in the as-built and T7 HT conditions.

A large density of fine dimples (approximately the same size of grains) is observed on the fracture surface of the LPBF A205 (as-built) material (Fig. 12a). This is an indication of typical ductile fracture with large strain to fracture capacity (see Fig. 4). A higher magnification SEM image of the as-built material shows Cu-rich and Ti-rich precipitates on the bottom of the dimples. When it comes to the LPBF A205 (T7 HT) fracture surface, though dimple structure is there, the presence of pre-existing pores, acting as stress intensifies, is more pronounced, Fig. 12b, limiting the ductility of the LPBF A205 (T7 HT) relative to the LPBF A205 (as-built) material.

The fracture surface of the cast materials shows the coarse distribution of dimples with the accumulation of some TiB_2 clusters and Al_2Cu particles inside the dimples (see Fig. 13a& b). The coarse crystals/particles are weak sites that readily de-bond from the α-aluminum matrix during mechanical testing. Coarse dimples, debonding, and microcracks contribute to the lower ductility of the cast relative to the LPBF A205 counter materials. Some inter-granular/*trans*-granular cracks are observed on the fracture surface of the as-cast material (shown with yellow arrows in Fig. 13a), which is responsible for the very limited ductility of the cast A205 (as-cast) specimen relative to the cast A205 (T7 T7) material where no obvious cracking was observed on the fracture surface.

4. Summary

In the present research, a comprehensive study was performed on the tensile behavior of A205 alloy, fabricated via LPBF and investment casting, to compare and correlate the process-induced microstructure with the tensile stress-strain flow curves of the materials. The main findings are listed here:

- Low work hardening rate, upper yield point, limited plastic flow instabilities, and appreciable elongation were observed in the tensile curves of the LPBF materials.
- Upon T7 heat treatment on the LPBF material, strength improves substantially, the yield point phenomenon disappears, and some PLC effect is observed.
- Unlike the LPBF material, limited ductility with no traces of PLC effect and no yield point phenomenon was observed in the cast counter material.
- The T7 heat treatment improves the ductility and strength of the cast-T7 relative to the as-cast material.
- Small dimples on the fracture surface of the LPBF materials relative to the presence of broken coarse precipitates, traces of debonding, and some microcracks on the fracture surfaces of the cast counter

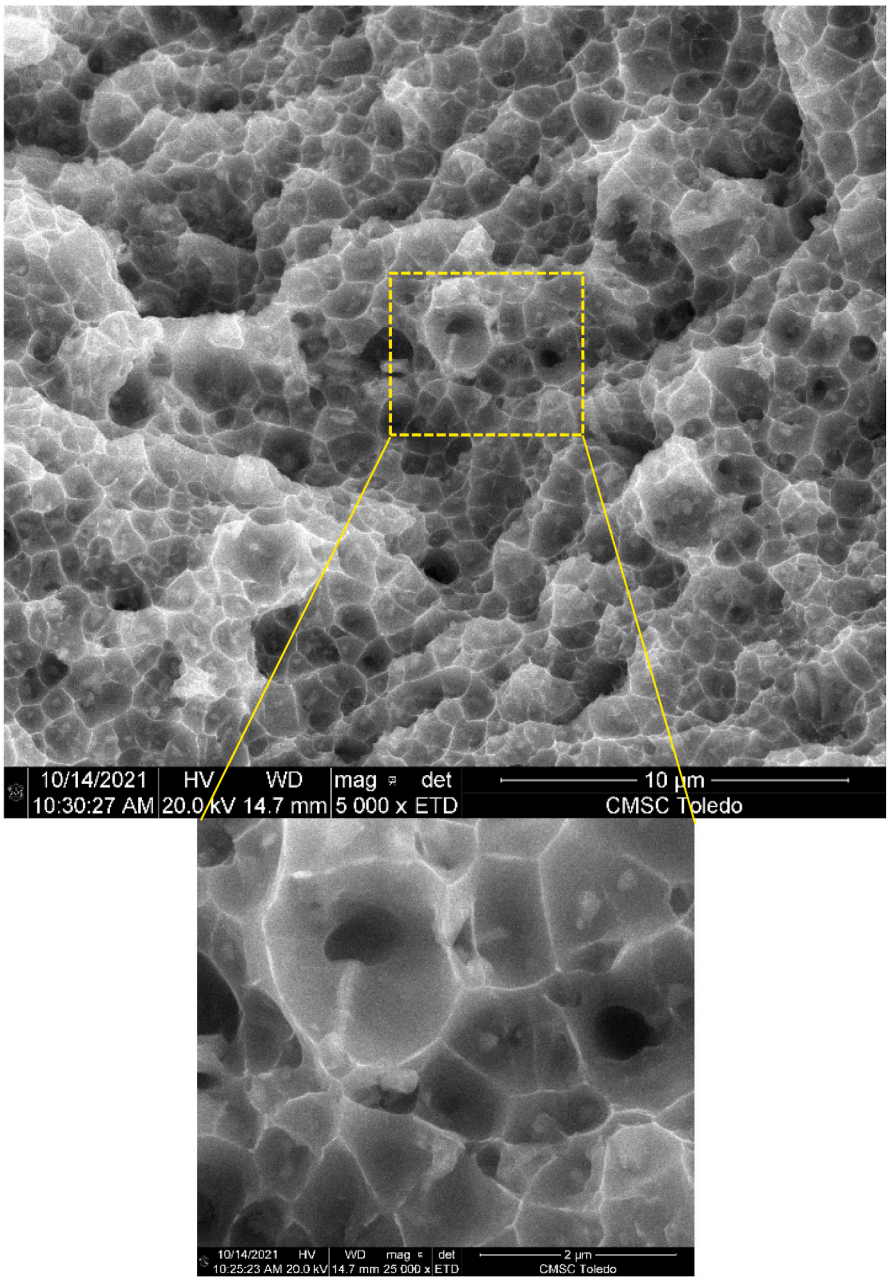

a

Fig. 12. SEM fractography images showing dimple features and pores on the fracture surfaces of LPBF A205 in the a) as-built and b) T7 HT condition.

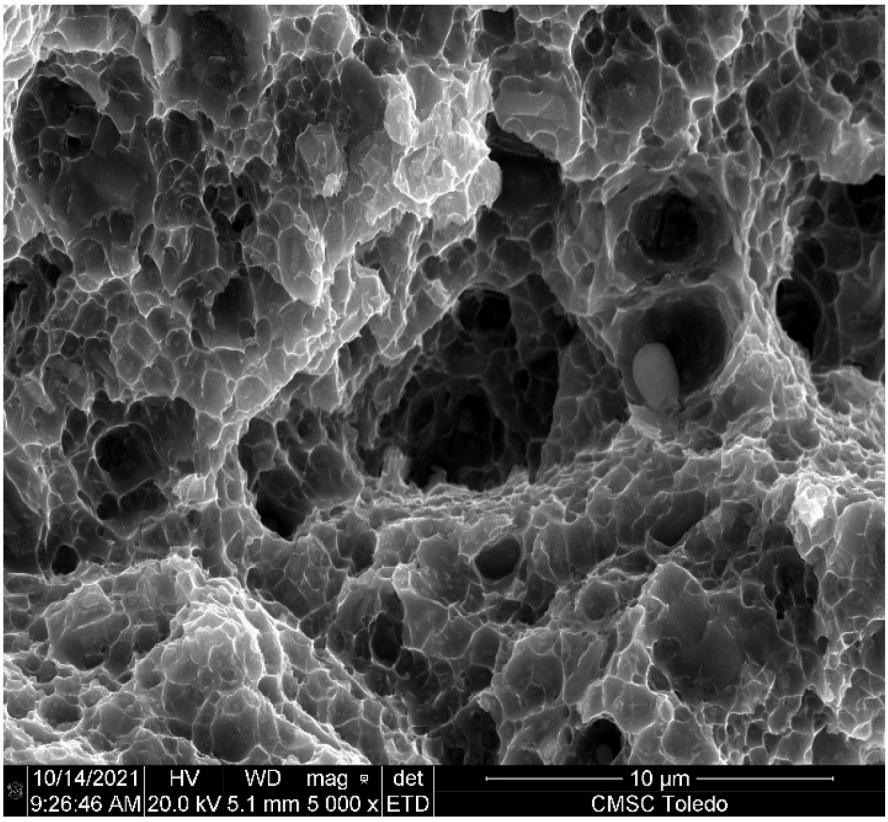

b

Fig. 12. (*continued*).

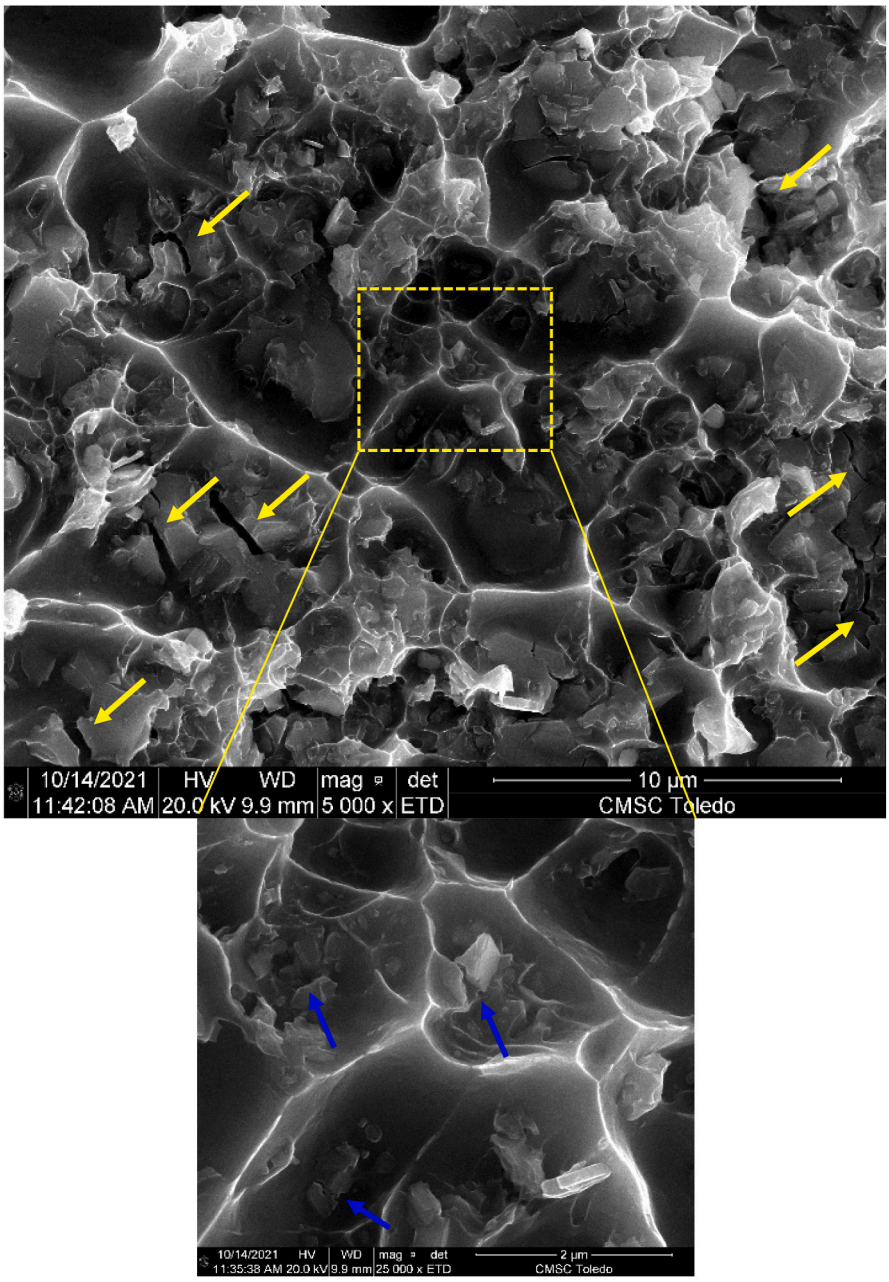

a

Fig. 13. SEM fractography of a) as-cast A205, b) cast-T7 A205 including microcracks on the fracture surface along with broken coarse Al–Cu particles.

materials confirm the enhanced ductility of LPBF materials relative to the cast counter materials.

Data availability

The raw/processed data required to reproduce these findings cannot be shared at this time as the data also forms part of an ongoing study.

CRediT authorship contribution statement

M. Avateffazeli: Writing – original draft. **P.E. Carrion:** Methodology. **B. Shachi-Amirkhiz:** Methodology, Writing – review & editing. **H. Pirgazi:** Methodology. **M. Mohammadi:** Writing – review & editing. **N. Shamsaei:** Writing – review & editing, Resources. **M. Haghshenas:** Resources, Conceptualization, Supervision.

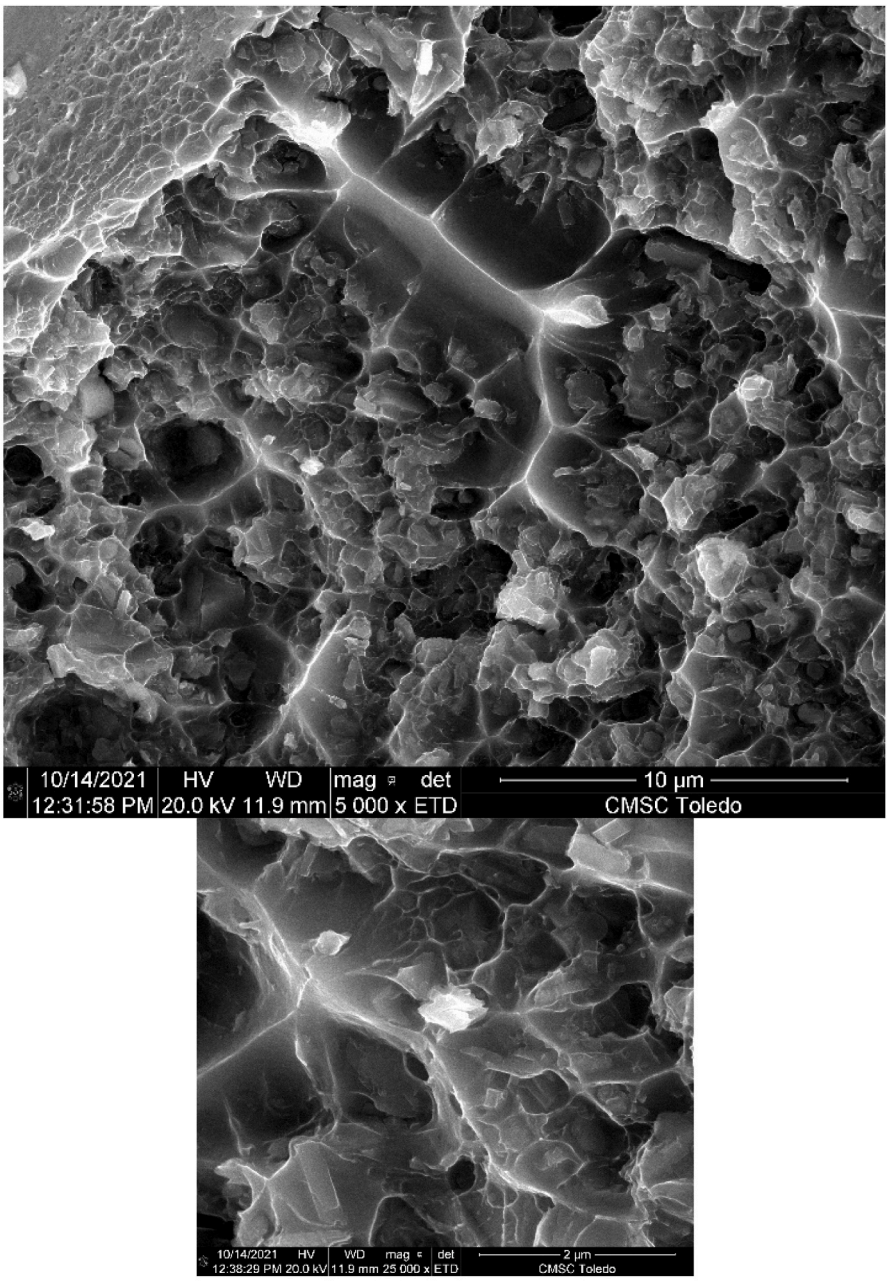

b

Fig. 13. (*continued*).

Declaration of competing interest

The authors declare that they have no known competing financial interests or personal relationships that could have appeared to influence the work reported in this paper.

Acknowledgment

The last author would like to acknowledge the great support of Mr. Mike Bond (Aluminum Materials Technologies Ltd.), Mr. William Stott (AMT Ltd., ECKART GmbH), Mr. Trevor Illston (Material Solutions), and Dr. Martin McMahon (Sandvik Additive Manufacturing) in providing the test materials and offering constructive comments on the results. The last author would like to also acknowledge the University Research Funding Opportunities (URFO UToledo) grant.

References

[1] Y. Gao, C. Yang, J. Zhang, L. Cao, G. Liu, J. Sun, E. Ma, Stabilizing nanoprecipitates in Al-Cu alloys for creep resistance at 300° C, Mater. Res. Lett. 7 (1) (2019) 18–25.
[2] L. Ravkov, B. Diak, M. Gallerneault, P. Clark, G. Marzano, The role of cooling rate on microstructure in a sand-cast Al-Cu–Ag alloy containing high amounts of TiB2, Canad. Metallurg. Quart. (2021) 1–9.
[3] M. Indriyati, Effect of TiB2 Addition on the Microstructure and Mechanical Properties of Al-Cu-Mg-Ag Alloy, 2016.
[4] M. Zamani, I. Belov, E. Sjölander, A. Bjurenstedt, E. Ghassemali, S. Seifeddine, Study on dissolution of Al2Cu in al-4.3 cu and a205 cast alloys, Metals 10 (7) (2020) 900.
[5] A. Hekmat-Ardakan, E.M. Elgallad, F. Ajersch, X.G. Chen, Microstructural evolution and mechanical properties of as-cast and T6-treated AA2195 DC cast alloy, Mater. Sci. Eng., A 558 (2012) 76–81.
[6] A. Kordijazi, D. Weiss, S. Das, S. Behera, H.M. Roshan, P. Rohatgi, Effect of solidification time on microstructure, wettability, and corrosion properties of A205-T7 aluminum alloys, Int. J. Metalcast. 15 (1) (2021) 2–12.
[7] S.I. Shakil, A.S. Zoeram, M. Avateffazeli, M. Roscher, H. Pirgazi, B. Shalchi-Amirkhiz, B. Poorganji, M. Mohammadi, M. Haghshenas, Ambient-temperature time-dependent deformation of cast and additive manufactured Al-Cu-Mg-Ag-TiB2 (A205), Micron (2022), 103246, https://doi.org/10.1016/j.micron.2022.103246.
[8] C.A. Biffi, P. Bassani, J. Fiocchi, M. Albu, A. Tuissi, Selective laser melting of AlCu-TiB2 alloy using pulsed wave laser emission mode: processability, microstructure and mechanical properties, Mater. Des. 204 (2021) 109628.
[9] X.P. Li, G. Ji, Z. Chen, A. Addad, Y. Wu, H.W. Wang, J. Vleugels, J. Van Humbeeck, J.-P. Kruth, Selective laser melting of nano-TiB2 decorated AlSi10Mg alloy with high fracture strength and ductility, Acta Mater. 129 (2017) 183–193.
[10] L. Xi, D. Gu, S. Guo, R. Wang, K. Ding, K.G. Prashanth, Grain refinement in laser manufactured Al-based composites with TiB2 ceramic, J. Mater. Res. Technol. 9 (3) (2020) 2611–2622.
[11] Q. Jia, P. Rometsch, P. Kürnsteiner, Q. Chao, A. Huang, M. Weyland, L. Bourgeois, X. Wu, Selective laser melting of a high strength AlMnSc alloy: alloy design and strengthening mechanisms, Acta Mater. 171 (2019) 108–118.
[12] M.H. Ghoncheh, M. Sanjari, A.S. Zoeram, E. Cyr, B.S. Amirkhiz, A. Lloyd, M. Haghshenas, M. Mohammadi, On the microstructure and solidification behavior of new generation additively manufactured Al-Cu-Mg-Ag-Ti-B alloys, Addit. Manuf. 37 (2021) 101724.
[13] P. Mair, V.S. Goettgens, T. Rainer, N. Weinberger, I. Letofsky-Papst, S. Mitsche, G. Leichtfried, Laser powder bed fusion of nano-CaB6 decorated 2024 aluminum alloy, J. Alloys Compd. 863 (2021) 158714.
[14] P. Mair, L. Kaserer, J. Braun, N. Weinberger, I. Letofsky-Papst, G. Leichtfried, Microstructure and mechanical properties of a TiB2-modified Al–Cu alloy processed by laser powder-bed fusion, Mater. Sci. Eng., A 799 (2021) 140209.
[15] X. Nie, H. Zhang, H. Zhu, Z. Hu, Y. Qi, X. Zeng, On the role of Zr content into Portevin-Le Chatelier (PLC) effect of selective laser melted high strength Al-Cu-Mg-Mn alloy, Mater. Lett. 248 (2019) 5–7.
[16] H. Zhang, H. Zhu, X. Nie, J. Yin, Z. Hu, X. Zeng, Effect of Zirconium addition on crack, microstructure and mechanical behavior of selective laser melted Al-Cu-Mg alloy, Scripta Mater. 134 (2017) 6–10.
[17] Z. Hu, Y. Qi, S. Gao, X. Nie, H. Zhang, H. Zhu, X. Zeng, Aging responses of an Al-Cu alloy fabricated by selective laser melting, Addit. Manuf. 37 (2021) 101635.
[18] S.I. Shakil, A.S. Zoeram, H. Pirgazi, B. Shalchi-Amirkhiz, B. Poorganji, M. Mohammadi, M. Haghshenas, Microstructural-micromechanical correlation in an Al–Cu–Mg–Ag–TiB2 (A205) alloy: additively manufactured and cast, Mater. Sci. Eng., A 832 (2022) 142453.
[19] Y.K. Xiao, H. Chen, Z.Y. Bian, T.T. Sun, H. Ding, Q. Yang, Y. Wu, Q. Lian, Z. Chen, H.W. Wang, Enhancing strength and ductility of AlSi10Mg fabricated by selective laser melting by TiB2 nanoparticles, J. Mater. Sci. Technol. 109 (2022) 254–266.
[20] D.D. Ben, Y.R. Ma, H.J. Yang, L.X. Meng, X.H. Shao, H.Q. Liu, S.G. Wang, Q. Q. Duan, Z.F. Zhang, Heterogeneous microstructure and voids dependence of tensile deformation in a selective laser melted AlSi10Mg alloy, Mater. Sci. Eng., A 798 (2020) 140109.
[21] H. Wu, G. Fan, An overview of tailoring strain delocalization for strength-ductility synergy, Prog. Mater. Sci. 113 (2020) 100675.
[22] Y. Xue, Q. Hao, B. Li, X. Wang, C. Yin, H. Zhang, Improving the strength-ductility trade-off of TiB2/Al-4.5% Cu composites via Mg–Ag microalloying and multi-step heat treatment, Mater. Res. Express 8 (5) (2021), 056519.
[23] J. Chen, C. Liu, Q. Li, M. Yao, Q. Zhou, H. Zhao, Stress aging of Al–Cu–Mg–Ag single crystal: the effect of the loading orientations, J. Alloys Compd. 816 (2020) 152635.
[24] Z. Mei, Z. Liu, S. Bai, J. Wang, J. Cao, Effects of yttrium additions on microstructures and mechanical properties of cast Al-Cu-Mg-Ag alloys, J. Alloys Compd. 870 (2021) 159435.
[25] X. Deng, Precipitation strengthening of stress-aged Al-Cu-Mg-Ag alloy single crystals, Mater. Sci. Eng., A (2021) 141458.
[26] S. Bai, H. Xu, Z. Liu, X. Yi, J. Zhao, J. Wang, On the role of the solute partitioning and chemistry in initial precipitation of Ω plates, Mater. Sci. Eng., A 766 (2019) 138339.
[27] S. Bai, P. Ying, Z. Liu, J. Wang, J. Li, Quantitative transmission electron microscopy and atom probe tomography study of Ag-dependent precipitation of Ω phase in Al-Cu-Mg alloys, Mater. Sci. Eng., A 687 (2017) 8–16.
[28] E. Gariboldi, P. Bassani, M. Albu, F. Hofer, Presence of silver in the strengthening particles of an Al-Cu-Mg-Si-Zr-Ti-Ag alloy during severe overaging and creep, Acta Mater. 125 (2017) 50–57.
[29] D.-y. Liu, J.-x. Wang, J.-f. Li, Y.-l. Ma, K. Zhang, R.-f. Zhang, The effect of Ag element on the microstructure characteristic evolution of an Al–Cu–Li–Mg alloy, J. Mater. Res. Technol. 9 (5) (2020) 11121–11134.
[30] E. Ma, T. Zhu, Towards strength–ductility synergy through the design of heterogeneous nanostructures in metals, Mater. Today 20 (6) (2017) 323–331.
[31] Y. Wang, M. Chen, F. Zhou, E. Ma, High tensile ductility in a nanostructured metal, Nature 419 (6910) (2002) 912–915.
[32] M. Gazizov, R. Kaibyshev, Precipitation structure and strengthening mechanisms in an Al-Cu-Mg-Ag alloy, Mater. Sci. Eng., A 702 (2017) 29–40.
[33] L. Zhan, X. Wu, X. Wang, Y. Yang, G. Liu, Y. Xu, Effect of process parameters on fatigue and fracture behavior of Al-Cu-Mg alloy after creep aging, Metals 8 (5) (2018) 298.
[34] I. Raffeis, F. Adjei-Kyeremeh, U. Vroomen, S. Richter, A. Bührig-Polaczek, Characterising the microstructure of an additively built Al-Cu-Li alloy, Materials 13 (22) (2020) 5188.
[35] X.-K. Yang, B.-Q. Xiong, X.-W. Li, L.-Z. Yan, Z.-H. Li, Y.-A. Zhang, Y.-N. Li, K. Wen, Effect of the addition of high Li concentration on the microstructure and mechanical properties of Al–Mg–Si alloys with different Mg contents, Acta Metall. Sin. (2021) 1–13.
[36] F. Jiang, J. Huang, Y. Jiang, C. Xu, Effects of quenching rate and over-aging on microstructures, mechanical properties and corrosion resistance of an Al–Zn–Mg (7046A) alloy, J. Alloys Compd. 854 (2021) 157272.
[37] J. Geng, G. Liu, T. Hong, M. Wang, D. Chen, N. Ma, H. Wang, Tuning the microstructure features of in-situ nano TiB2/Al-Cu-Mg composites to enhance mechanical properties, J. Alloys Compd. 775 (2019) 193–201.
[38] Z. Wang, M. Xie, Y. Li, W. Zhang, C. Yang, L. Kollo, J. Eckert, K.G. Prashanth, Premature failure of an additively manufactured material, NPG Asia Mater. 12 (1) (2020) 1–10.
[39] J. Kacher, B.P. Eftink, B. Cui, I.M. Robertson, Dislocation interactions with grain boundaries, Curr. Opin. Solid State Mater. Sci. 18 (4) (2014) 227–243.
[40] C. Shao, S. Zhao, X. Wang, Y. Zhu, Z. Zhang, R.O. Ritchie, Architecture of high-strength aluminum–matrix composites processed by a novel microcasting technique, NPG Asia Mater. 11 (1) (2019) 1–12.